AIAA JOURNAL
Vol. 39, No. 11, November 2001

Higher-Order Solution Procedure for Three-Dimensional Nonideal Magnetogasdynamics

Datta V. Gaitonde*
U.S. Air Force Research Laboratory, Wright–Patterson Air Force Base, Ohio 45433

A high-resolution scheme developed for use in multidisciplinary applications is applied to solve the equations governing the three-dimensional flow of a nonideal compressible conducting fluid in a magnetic field. Both 4th-order and 6th-order spatially implicit schemes are considered in conjunction with up to 10th-order filters. The fourth-order classical Runge–Kutta scheme is employed for time integration. The accuracy and versatility of the algorithm and the accompanying code are explored by solving a wide variety of problems, discretized with uniform as well as curvilinear grids, with particular emphasis on the unique physical phenomena arising in conducting fluids. These phenomena include Alfvén wave propagation with and without ohmic damping, magnetic field diffusion, shock- and compound-wave formation, as well as interactions between pressure, viscous and electromagnetic forces of the kind occurring in magnetohydrodynamic brakes, flowmeters, generators, and accelerators.

Nomenclature

a, b	=	constants in differencing formula
$\boldsymbol{B}$	=	magnetic induction vector
C	=	complex coefficient
C_p	=	specific heat at constant pressure
$C4, C6$	=	fourth- and sixth-order formulas
c	=	speed of light; wave velocity
c_A	=	Alfvén wave velocity
D	=	electric displacement
E	=	electric field intensity
E_{em}	=	electromagnetic energy
$E2, E4$	=	second- and fourth-order explicit formulas
$\boldsymbol{F}, \boldsymbol{G}$	=	flux vectors
F_{em}	=	electromagnetic force
$\boldsymbol{H}$	=	flux vector, magnetic field intensity, height
Ha	=	Hartmann number
IL, JL, KL	=	number of mesh points
J	=	integrated current
j	=	current density
K	=	electric load factor
k	=	thermal conductivity
L	=	reference length
M	=	Mach number
n	=	along normal direction
P	=	sum of static and magnetic pressure
Pr	=	Prandtl number
p	=	static pressure
Q	=	heat flux
Q_f	=	flow rate
q	=	charge density
R	=	gas constant of medium; residual
R_b	=	magnetic force (or pressure) number
Re_σ	=	magnetic Reynolds number
T	=	temperature
t	=	time
$\boldsymbol{U}$	=	velocity vector
u, v, w	=	Cartesian components of velocity
W	=	width of channel
$\boldsymbol{X}$	=	vector of conserved variables
x, y, z	=	Cartesian coordinates
Z	=	sum of specific internal, kinetic, and magnetic energies
α_f	=	coefficient in filter formula
Γ	=	constant in differencing formula
γ	=	ratio of specific heats
Δ	=	difference operator
δ	=	small number
ϵ	=	dielectric constant
μ	=	molecular viscosity
μ_m	=	magnetic permeability
ξ, η, ζ	=	transformed coordinates
ρ	=	density
σ	=	conductivity
$\bar{\bar{\tau}}$	=	shear stress tensor
ϕ, Φ	=	generic scalar variable
χ	=	filter switch for shocks
ω	=	frequency

Subscripts

ref	=	reference values
v	=	viscous
w	=	wall
x, y, z	=	components or derivatives with respect to x, y, and z

Superscripts

$*$	=	nondimensional quantity
$'$	=	vectors in transformed coordinates; derivative

I. Introduction

THE effects associated with the interaction of magnetic forces with conducting fluid flows have been profitably employed in several applications related to nuclear and material processing technologies and are known to be essential in the explanation of astrophysical phenomena. The present effort is concerned with the use of these interactions in the control of hypersonic flows. In recent years, such studies have received fresh impetus in the effort to solve the problems of high drag and thermal loads encountered in hypersonic flight. The knowledge that electrical and magnetic forces can have a profound influence on hypersonic flowfields is not new, for example, Refs. 1 and 2 note increased shock-standoff and reduced heat transfer rates in hypersonic flows past blunt bodies under the influence of appropriate magnetic fields. The renewed interest stems, however, from revelations of a Russian concept vehicle, known as the AJAX,[3] based on technologies requiring tight coupling between electromagnetic and fluid dynamic phenomena. A magnetogasdynamic (MGD) generator was proposed[4] to extract energy from the incoming air while simultaneously enhancing fuel–air mixing

Received 16 July 2000; revision received 27 April 2001; accepted for publication 27 April 2001.

*Research Aerospace Engineer, Computational Sciences Branch, Aeronautical Sciences Division, Building 146, Room 225, 2210 Eighth Street; datta@vaa.wpafb.af.mil. Associate Fellow AIAA.

and providing more benign flow to the combustion components downstream. The extracted energy could then be employed to increase thrust by MGD pumping of the flow exiting the nozzle or to assist in the generation of a plasma for injection upstream of the body. Preliminary experimental data show that this latter technique may not only reduce drag on the body, but may also provide a significant degree of thermal protection.[5] Another field of budding current interest is based on the observation that turbulence can be potentially reduced through proper application of magnetic fields.[6] The implication of this possibility is also revolutionary because of the direct connection between turbulence and vehicle loading. Resolution of these issues, from both the scientific and engineering standpoints, will require extensive experimentation as well as high-fidelity simulation efforts. The latter approach requires integration of several disciplines, including fluid dynamics, electromagnetics, chemical kinetics, and molecular physics, among others. This paper describes a recent effort to integrate the first two of these, within the assumptions that characterize nonideal MGD.

Recent research in the development of algorithms to solve the equations of continuum MGD has focused primarily on the derivation of the proper eigensystem to provide a framework for an upwind or characteristic-based scheme. Examples of such efforts may be found in Refs. 7–9. These schemes solve a Riemann problem, generally in the direction normal to a cell face, to obtain the fluxes in a finite volume formulation. An evaluation of such schemes in the context of nonmagnetohydrodynamics (non-MHD) flows has been presented in Refs. 10 and 11. Characteristic-based schemes have been incorporated into two-dimensional and axisymmetric codes for both ideal[12,13] and nonideal[14,15] situations.

The numerical scheme employed in the present effort differs from those in previous MGD research in that it is based on very high-order-accurate compact (Padé-type) formulas.[16,17] These difference schemes are coupled with a corresponding set of appropriately high-order accurate filters that are required to enforce numerical stability. Both 4th- and 6th-order approaches are considered for the difference scheme, whereas the filtering schemes of up to 10th order are taken from Refs. 18 and 19. The method does not require a priori knowledge of the eigensystem. Because its development is independent of the specific equation set under consideration, it is amenable to multidisciplinary application with relatively little additional effort. Indeed, variants of the compact difference and filter formulas employed here were originally developed to solve Maxwell's equations[18] and were subsequently employed without significant modification to solve the full three-dimensional Navier–Stokes equations[10] for problems ranging from turbulence[20,21] to acoustics.[11] The flexibility and versatility afforded by this approach is an important asset in the long-term goal of obtaining high-fidelity numerical solutions to the complex equations associated with advanced models of plasmas.

Although studies with ideal, perfectly conducting fluids are useful in several situations, most notably in astrophysics, the approximation is not appropriate for typical flows encountered in aerospace applications, except at extremely high altitudes and Mach numbers. Without difficult and expensive artificial augmentation, conductivity is far from perfect in that part of the flight envelope characterized by weakly ionized regimes. Furthermore, variability of conduction can have a significant impact on the performance of practical devices (see, for example, Ref. 22). The present work, therefore, considers the nonideal equations in which both the magnetic, as well as viscous, diffusion terms are retained in general form. We also focus on developing a code and methodology for the full three-dimensional case. For MGD, reduction to two space dimensions is known to yield features whose characteristics and stability are entirely different in the full three-dimensional analysis.[23]

Several levels of approximations exist in the simulation of MGD problems. Section II elucidates those employed in this work by developing the governing equations for the three-dimensional flow of a nonideal compressible conducting gas. The equations are rewritten in nondimensional flux-vector form for use in general curvilinear coordinate discretizations. A brief description of the numerical scheme employed is presented in Sec. III. The method is then validated by considering several test cases in Sec. IV with emphasis on the ability of the method to resolve the new phenomena arising in conducting fluids under the influence of magnetic fields.

II. Physical Model

A. Governing Equations

The governing equations of MGD are obtained by coupling the pre-Maxwell equations to the Navier–Stokes equations through the momentum and energy equations. The complete Maxwell equations may be written, in SI units, as[24]

$$\nabla \times \boldsymbol{H} = \boldsymbol{j} + \frac{\partial D}{\partial t} \tag{1}$$

$$\nabla \times \boldsymbol{E} = -\frac{\partial \boldsymbol{B}}{\partial t} \tag{2}$$

$$\nabla \cdot B = 0 \tag{3}$$

$$\nabla \cdot D = q \tag{4}$$

where H and E are the magnetic and electric field vectors, D is the electric displacement, B is the magnetic induction vector, j is the current density vector, and q is the charge density. Equation (1) represents the Ampere–Maxwell law and Eq. (2) is Faraday's law. Two important assumptions in the study of MGD are 1) $\epsilon\omega/\sigma \ll 1$ and 2) $(|U|/c)^2 \ll 1$, where ϵ is the dielectric constant, ω is a representative frequency of interest, σ is the electrical conductivity, $U = \{u, v, w\}$ is the velocity of the conducting medium, and c is the speed of light. The first of these two assumptions permits the simplification that results from discarding the displacement current, $\partial D/\partial t$ from the Ampere–Maxwell law. The resulting set of equations is sometimes termed pre-Maxwell. The second assumption permits relativistic effects to be ignored. Then, the constitutive equations relating $\boldsymbol{B}, \boldsymbol{H}, \boldsymbol{E}$, and $\boldsymbol{j}$ for the medium, written in the laboratory frame of reference, may be assumed to be

$$\boldsymbol{B} = \mu_m \boldsymbol{H} \tag{5}$$

$$\boldsymbol{j} = \sigma(\boldsymbol{E} + U \times \boldsymbol{B}) \tag{6}$$

where μ_m is the magnetic permeability and, in Eq. (6) (Ohm's law), the convection, polarization, Hall, and ion-slip current components have been neglected. The analysis is, thus, pertinent to strongly collision dominated plasmas. When $\boldsymbol{E}$ is eliminated from Ohm's and Faraday's laws and $\boldsymbol{j}$ is subsequently eliminated with Ampere's law, with Eqs. (3) and (5), the equation describing the evolution of the magnetic induction vector may be written as

$$\frac{\partial \boldsymbol{B}}{\partial t} + \nabla \times \left[\frac{1}{\sigma} \left(\nabla \times \frac{\boldsymbol{B}}{\mu_m} \right) - U \times \boldsymbol{B} \right] = 0 \tag{7}$$

or, equivalently, in effective conservation form, as

$$\frac{\partial \boldsymbol{B}}{\partial t} + \nabla \cdot (\bar{\bar{U}}\boldsymbol{B} - \boldsymbol{B}\bar{\bar{U}}) + \nabla \times \left[\frac{1}{\sigma} \left(\nabla \times \frac{\boldsymbol{B}}{\mu_m} \right) \right] = 0 \tag{8}$$

where the dyadic is denoted with the double overbar. Equation (8) exhibits a great deal of similarity with the vorticity equation and includes phenomena associated with convection, stretching, and diffusion of the $\boldsymbol{B}$ field.

The equations describing fluid motion are the Navier–Stokes equations. The continuity equation remains unchanged:

$$\frac{\partial \rho}{\partial t} + \nabla \cdot (\rho U) = 0 \tag{9}$$

where ρ is the density. The momentum equation contains the extra electromagnetic body force term $F_{\text{em}} = \boldsymbol{j} \times \boldsymbol{B}$, which may be expressed in the form of Maxwell's stresses by noting that

$$F_{\text{em}} = j \times \boldsymbol{B} = (\nabla \times \boldsymbol{B}/\mu_m) \times \boldsymbol{B} = (\boldsymbol{B} \cdot \nabla)(\boldsymbol{B}/\mu_m) - \nabla \cdot \left(\boldsymbol{B}^2/2\mu_m\right) = \nabla(\bar{\bar{B}}\boldsymbol{B}/\mu_m) - \nabla \cdot \left(\boldsymbol{B}^2/2\mu_m\right)$$

where $\nabla \cdot \boldsymbol{B} = 0$ has been employed. The momentum equation is, therefore,

$$\frac{\partial \rho U}{\partial t} + \nabla \cdot \left[\rho U\bar{U} - \frac{\bar{\bar{B}}\boldsymbol{B}}{\mu_m} + P\bar{\bar{I}}\right] - \nabla \cdot \bar{\bar{\tau}} = 0 \tag{10}$$

$P = p + (\boldsymbol{B}^2/2\mu_m)$ is the sum of the static p and magnetic pressures, $\bar{\bar{I}}$ is the identity tensor, and $\bar{\bar{\tau}}$ is the shear stress tensor defined in terms of the molecular viscosity μ by

$$\bar{\bar{\tau}} = \begin{bmatrix} \frac{2}{3}\mu(2u_x - v_y - w_z) & \mu(u_y + v_x) & \mu(u_z + w_x) \\ \mu(u_y + v_x) & \frac{2}{3}\mu(2v_y - u_x - w_z) & \mu(v_z + w_y) \\ \mu(u_z + w_x) & \mu(v_z + w_y) & \frac{2}{3}\mu(2w_z - u_x - v_y) \end{bmatrix}$$

The energy equation is modified by the addition of the electromagnetic energy term E_{em}

$$\boldsymbol{E}_{\text{em}} = \boldsymbol{E} \cdot \boldsymbol{j} = -(U \times \boldsymbol{B}) \cdot (\nabla \times \boldsymbol{B}/\mu_m) + (\nabla \times \boldsymbol{B}/\mu_m) \cdot 1/\sigma(\nabla \times \boldsymbol{B}/\mu_m)$$

in which the last expression is recognizable as the Joule heating term, $\boldsymbol{j}^2/\sigma$, by virtue of Ampere's law. The energy equation may be derived in convenient conservation law form by introducing the variable $Z = e + (\boldsymbol{B} \cdot \boldsymbol{B})/2\mu_m\rho$ where $e = [p/(\gamma - 1)\rho] + \frac{1}{2}U \cdot U$:

$$\frac{\partial \rho Z}{\partial t} + \nabla \cdot \left[(\rho Z + P)U - B\left(U \cdot \frac{\boldsymbol{B}}{\mu_m}\right) - U \cdot \bar{\bar{\tau}} - Q + \left(\frac{\boldsymbol{B}}{\mu_m\sigma} \cdot \nabla\frac{\bar{\bar{B}}}{\mu_m} - \nabla\frac{\bar{\bar{B}}}{\mu_m} \cdot \frac{\boldsymbol{B}}{\mu_m\sigma}\right)\right] = 0 \tag{11}$$

Q is the heat flux related to the thermal conductivity k and the temperature T through $Q = k\nabla T$. The pressure p is related to the temperature with the perfect gas equation of state, $p = \rho RT$, where R is the gas constant of the medium. Here, γ is the ratio of specific heats, and Sutherland's law is employed to obtain the molecular viscosity μ.

B. Nondimensionalization

The equations are nondimensionalized by the quantities ρ_{ref}, U_{ref}, the length scale L, B_{ref}, $\mu_{m_{\text{ref}}}$, μ_{ref}, T_{ref}, and σ_{ref}. The nondimensional variables are then

$$t^* = tL/U_{\text{ref}}, \quad \rho^* = \rho/\rho_{\text{ref}}, \quad U^* = U/U_{\text{ref}}, \quad \boldsymbol{B}^* = \boldsymbol{B}/B_{\text{ref}}, \quad p^* = p/\rho_{\text{ref}}U_{\text{ref}}^2, \quad \mu_m^* = \mu_m/\mu_{m_{\text{ref}}}, \quad \mu^* = \mu/\mu_{\text{ref}}, \quad \sigma^* = \sigma/\sigma_{\text{ref}}, \quad T^* = T/T_{\text{ref}} \tag{12}$$

and the governing equations (8–11) are transformed into

$$\frac{\partial \rho^*}{\partial t^*} + \nabla \cdot (\rho^* U^*) = 0 \tag{13}$$

$$\frac{\partial \rho^* U^*}{\partial t^*} + \nabla \cdot \left[\rho^* U^*\bar{U}^* - R_b\frac{\bar{\bar{B}}^*\boldsymbol{B}^*}{\mu_m} + P^*\bar{\bar{I}}\right] - \frac{1}{Re}\nabla \cdot \bar{\bar{\tau}}^* = 0 \tag{14}$$

$$\frac{\partial \rho^* Z^*}{\partial t^*} + \nabla \cdot \left[(\rho^* Z^* + P^*)U - R_b\boldsymbol{B}^*\left(U^* \cdot \frac{\boldsymbol{B}^*}{\mu_m^*}\right) - \frac{1}{Re}(U^* \cdot \bar{\bar{\tau}}^*) - \frac{1}{(\gamma - 1)PrM^2Re}Q^* + \frac{R_b}{R_\sigma}\left(\frac{\boldsymbol{B}^*}{\mu_m^*\sigma^*} \cdot \nabla\frac{\bar{\bar{B}}^*}{\mu_m^*} - \nabla\frac{\bar{\bar{B}}^*}{\mu_m^*} \cdot \frac{\boldsymbol{B}^*}{\mu_m^*}\sigma^*\right)\right] = 0 \tag{15}$$

$$\frac{\partial \boldsymbol{B}^*}{\partial t^*} + \nabla \cdot \left(U^*\bar{\bar{B}}^* - \boldsymbol{B}^*\bar{U}^*\right) + \frac{1}{Re_\sigma}\nabla \times \left[\frac{1}{\sigma^*}\left(\nabla \times \frac{\boldsymbol{B}^*}{\mu_m^*}\right)\right] = 0 \tag{16}$$

where $Q^* = \nabla T^*$, $\bar{\bar{\tau}}^*$ is obtained from $\bar{\bar{\tau}}$ by simply replacing each component with its nondimensional equivalent, and

$$P^* = p^* + R_b\left(\boldsymbol{B}^{*^2}/2\mu_m^*\right) \tag{17}$$

$$Z^* = p^*/(\gamma - 1)\rho^* + U^{*^2}/2 + R_b\left(\boldsymbol{B}^{*^2}/2\mu_m^*\rho^*\right) \tag{18}$$

$Re = \rho_{\text{ref}}U_{\text{ref}}L/\mu_{\text{ref}}$ is the Reynolds number, $R_b = B_{\text{ref}}^2/\rho_{\text{ref}}U_{\text{ref}}^2\mu_{m_{\text{ref}}}$ is the magnetic force (or pressure) number, $Re_\sigma = LU_{\text{ref}}\mu_{m_{\text{ref}}}\sigma_{\text{ref}}$ is the magnetic Reynolds number, $Pr = \mu_{\text{ref}}C_p/k = 0.72$ is the Prandtl number, and $M = U_{\text{ref}}/\sqrt{(\gamma p/\rho)}$ is the Mach number. For notational convenience, the asterisk superscript will be dropped in the subsequent discussion, and all quantities will be assumed to be nondimensional unless explicitly stated otherwise.

C. Flux-Vector Form

In Cartesian coordinates, the preceding equations may be written in flux-vector form as

$$\frac{\partial \boldsymbol{X}}{\partial t} + \frac{\partial \boldsymbol{F}}{\partial x} + \frac{\partial \boldsymbol{G}}{\partial y} + \frac{\partial \boldsymbol{H}}{\partial z} = \frac{\partial \boldsymbol{F}_v}{\partial x} + \frac{\partial \boldsymbol{G}_v}{\partial y} + \frac{\partial \boldsymbol{H}_v}{\partial z} \tag{19}$$

where $\boldsymbol{X}$ is the solution vector, $\boldsymbol{X} = \{\rho, \rho u, \rho v, \rho w, \rho Z, B_x, B_y, B_z\}$; $\boldsymbol{F}$, $\boldsymbol{G}$, and $\boldsymbol{H}$ contain terms relevant to inviscid, perfectly conducting media; and $\boldsymbol{F}_v$, $\boldsymbol{G}_v$, and $\boldsymbol{H}_v$ include effects due to viscosity and finite electrical conductivity. The various vectors of Eq. (19) are

$$\boldsymbol{F} = \begin{Bmatrix} \rho u \\ \rho u^2 + P - R_b\left(B_x^2/\mu_m\right) \\ \rho uv - R_bB_x(B_y/\mu_m) \\ \rho uw - R_bB_x(B_z/\mu_m) \\ (\rho Z + P)u - R_b(U \cdot B/\mu_m)B_x \\ 0 \\ uB_y - vB_x \\ uB_z - wB_x \end{Bmatrix} \tag{20}$$

$$\boldsymbol{G} = \begin{Bmatrix} \rho v \\ \rho uv - R_bB_x(B_y/\mu_m) \\ \rho v^2 + P - R_b\left(B_y^2/\mu_m\right) \\ \rho vw - R_bB_y(B_z/\mu_m) \\ (\rho Z + P)v - R_b(U \cdot B/\mu_m)B_y \\ vB_x - uB_y \\ 0 \\ vB_z - wB_y \end{Bmatrix} \tag{21}$$

$$\boldsymbol{H} = \begin{Bmatrix} \rho v \\ \rho u w - R_b B_x (B_z/\mu_m) \\ \rho v w - R_b B_y (B_z/\mu_m) \\ \rho w^2 + P - R_b \left(B_z^2/\mu_m\right) \\ (\rho Z + P) w - R_b (U \cdot B/\mu_m) B_z \\ w B_x - u B_z \\ w B_y - v B_z \\ 0 \end{Bmatrix} \tag{22}$$

$$\boldsymbol{F}_v = \begin{Bmatrix} 0 \\ \frac{1}{Re}\tau_{xx} \\ \frac{1}{Re}\tau_{xy} \\ \frac{1}{Re}\tau_{xz} \\ \hline \frac{1}{Re}(u\tau_{xx} + v\tau_{xy} + w\tau_{xz}) + \frac{1}{(\gamma-1)PrM^2Re}\frac{\partial T}{\partial x} \\ \quad + \frac{R_b}{R_\sigma}\left\{ \frac{B_y}{\mu_m \sigma}\left(\frac{\partial}{\partial x}\frac{B_y}{\mu_m} - \frac{\partial}{\partial y}\frac{B_x}{\mu_m} \right) \right. \\ \quad \left. + \frac{B_z}{\mu_m \sigma}\left(\frac{\partial}{\partial x}\frac{B_z}{\mu_m} - \frac{\partial}{\partial z}\frac{B_x}{\mu_m} \right) \right\} \\ \hline 0 \\ \frac{1}{Re_\sigma}\frac{1}{\sigma}\left(\frac{\partial}{\partial x}\frac{B_y}{\mu_m} - \frac{\partial}{\partial y}\frac{B_x}{\mu_m} \right) \\ \frac{1}{Re_\sigma}\frac{1}{\sigma}\left(\frac{\partial}{\partial x}\frac{B_z}{\mu_m} - \frac{\partial}{\partial z}\frac{B_x}{\mu_m} \right) \end{Bmatrix} \tag{23}$$

$$\boldsymbol{G}_v = \begin{Bmatrix} 0 \\ \frac{1}{Re}\tau_{xy} \\ \frac{1}{Re}\tau_{yy} \\ \frac{1}{Re}\tau_{yz} \\ \hline \frac{1}{Re}(u\tau_{xy} + v\tau_{yy} + w\tau_{yz}) + \frac{1}{(\gamma-1)PrM^2Re}\frac{\partial T}{\partial y} \\ \quad + \frac{R_b}{Re_\sigma}\left\{ \frac{B_x}{\mu_m \sigma}\left(\frac{\partial}{\partial y}\frac{B_x}{\mu_m} - \frac{\partial}{\partial x}\frac{B_y}{\mu_m} \right) \right. \\ \quad \left. + \frac{B_z}{\mu_m \sigma}\left(\frac{\partial}{\partial y}\frac{B_z}{\mu_m} - \frac{\partial}{\partial z}\frac{B_y}{\mu_m} \right) \right\} \\ \hline \frac{1}{Re_\sigma}\frac{1}{\sigma}\left(\frac{\partial}{\partial y}\frac{B_x}{\mu_m} - \frac{\partial}{\partial x}\frac{B_y}{\mu_m} \right) \\ 0 \\ \frac{1}{Re_\sigma}\frac{1}{\sigma}\left(\frac{\partial}{\partial y}\frac{B_z}{\mu_m} - \frac{\partial}{\partial z}\frac{B_y}{\mu_m} \right) \end{Bmatrix} \tag{24}$$

$$\boldsymbol{H}_v = \begin{Bmatrix} 0 \\ \frac{1}{Re}\tau_{xz} \\ \frac{1}{Re}\tau_{yz} \\ \frac{1}{Re}\tau_{zz} \\ \hline \frac{1}{Re}(u\tau_{xz} + v\tau_{yz} + w\tau_{zz}) + \frac{1}{(\gamma-1)PrM^2Re}\frac{\partial T}{\partial z} \\ \quad + \frac{R_b}{Re_\sigma}\left\{ \frac{B_x}{\mu_m \sigma}\left(\frac{\partial}{\partial z}\frac{B_x}{\mu_m} - \frac{\partial}{\partial x}\frac{B_z}{\mu_m} \right) \right. \\ \quad \left. + \frac{B_y}{\mu_m \sigma}\left(\frac{\partial}{\partial z}\frac{B_y}{\mu_m} - \frac{\partial}{\partial y}\frac{B_z}{\mu_m} \right) \right\} \\ \hline \frac{1}{Re_\sigma}\frac{1}{\sigma}\left(\frac{\partial}{\partial z}\frac{B_x}{\mu_m} - \frac{\partial}{\partial x}\frac{B_z}{\mu_m} \right) \\ \frac{1}{Re_\sigma}\frac{1}{\sigma}\left(\frac{\partial}{\partial z}\frac{B_y}{\mu_m} - \frac{\partial}{\partial y}\frac{B_z}{\mu_m} \right) \\ 0 \end{Bmatrix} \tag{25}$$

D. Extension to Curvilinear Coordinates

The governing equations are extended to curvilinear coordinates in the standard manner[25] by introducing the transformation $x = x(\xi, \eta, \zeta)$, $y = y(\xi, \eta, \zeta)$, and $z = z(\xi, \eta, \zeta)$. The strong conservation form is employed, transforming Eq. (19) to

$$\frac{\partial \boldsymbol{X}'}{\partial t} + \frac{\partial \boldsymbol{F}'}{\partial \xi} + \frac{\partial \boldsymbol{G}'}{\partial \eta} + \frac{\partial \boldsymbol{H}'}{\partial \zeta} = \frac{\partial \boldsymbol{F}'_v}{\partial \xi} + \frac{\partial \boldsymbol{G}'_v}{\partial \eta} + \frac{\partial \boldsymbol{H}'_v}{\partial \zeta} \tag{26}$$

where, with J representing the Jacobian of the transformation, $\boldsymbol{X}' = \boldsymbol{X}/J$ and

$$\boldsymbol{F}' = (1/J)(\xi_x \boldsymbol{F} + \xi_y \boldsymbol{G} + \xi_z \boldsymbol{H})$$

$$\boldsymbol{G}' = (1/J)(\eta_x \boldsymbol{F} + \eta_y \boldsymbol{G} + \eta_z \boldsymbol{H})$$

$$\boldsymbol{H}' = (1/J)(\zeta_x \boldsymbol{F} + \zeta_y \boldsymbol{G} + \zeta_z \boldsymbol{H})$$

$$\boldsymbol{F}'_v = (1/J)(\xi_x \boldsymbol{F}_v + \xi_y \boldsymbol{G}_v + \xi_z \boldsymbol{H}_v)$$

$$\boldsymbol{G}'_v = (1/J)(\eta_x \boldsymbol{F}_v + \eta_y \boldsymbol{G}_v + \eta_z \boldsymbol{H}_v)$$

$$\boldsymbol{H}' = (1/J)(\zeta_x \boldsymbol{F}_v + \zeta_y \boldsymbol{G}_v + \zeta_z \boldsymbol{H}_v)$$

III. Numerical Scheme

A finite difference approach is employed to discretize the preceding equations. Discrete quantities are, therefore, assumed to be pointwise in nature. This choice is motivated by the relative ease of formal extension to higher-order accuracy. All spatial derivatives are obtained with compact (or Padé-type) schemes. Thus, the derivative of any scalar quantity, for example, ϕ, is obtained in the uniformly discretized transformed plane (ξ, η, ζ) by solving the equation

$$\Gamma \phi'_{i-1} + \phi'_i + \Gamma \phi'_{i+1} = b[(\phi_{i+2} - \phi_{i-2})/4] + a[(\phi_{i+1} - \phi_{i-1})/2] \tag{27}$$

where Γ, a, and b determine the spatial properties of the algorithm. In this work, the primary focus is on the fourth-order compact scheme, denoted C4, for which $\Gamma = \frac{1}{4}$, $a = \frac{3}{2}$, and $b = 0$, and on the sixth-order scheme, C6, with $\Gamma = \frac{1}{3}$, $a = \frac{14}{9}$, and $b = \frac{1}{9}$. Note that when Γ is non-zero, a tridiagonal system needs to be solved. Two other schemes are also considered for comparison purposes, the standard explicit fourth-order E4 ($\Gamma = 0$, $a = \frac{4}{3}$, and $b = -\frac{1}{3}$) and second-order E2 ($\Gamma = 0$, $a = 1$, and $b = 0$). Dispersion characteristics, presented in Refs. 17 and 26, demonstrate the superiority of the compact schemes C4 and C6 over their explicit counterparts.

The preceding formula cannot be applied at endpoints 1 and IL for C4 and at 1, 2, $IL-1$, and IL for C6. At these points, higher-order one-sided formulas are utilized that retain the tridiagonal form of the equation set. These boundary schemes and coefficients may be obtained from various sources in the literature[27,28] and have been collectively reproduced in Ref. 29. The alternative approach of utilizing ghost points has not been pursued in this work.

The derivatives of the inviscid fluxes are obtained by first forming these fluxes at the nodes and subsequently obtaining derivatives for each component. To reduce the error on stretched meshes, the metrics are computed with the same scheme as that employed for the fluxes.[10,18,30] To form the nonideal terms containing the molecular viscosity μ and electrical conductivity σ, the primitive variables u, v, w, T, B_x, B_y, and B_z and are first differentiated and properly combined with the transport coefficients to form the requisite combinations of first derivative terms. These gradients are then differentiated again with the same difference scheme. Although this approach may not provide sufficient resistance to odd–even decoupling,[17] no difficulty has been noted so far in this and other efforts[10] because the filtering approach described hereafter guarantees the suppression of high-frequency modes.

Filtering is employed to maintain numerical stability in the presence of mesh nonuniformity, approximate boundary condition implementation, and in the capture of nonlinear phenomena. The filter is applied in a postprocessing manner to the solution vector $\boldsymbol{X}$, that is, after the update at each time step. Denoting a typical component of the solution vector by ϕ, filtered values $\hat{\phi}$ are obtained with the scheme

$$\alpha_f \hat{\phi}_{i-1} + \hat{\phi}_i + \alpha_f \hat{\phi}_{i+1} = \sum_{n=0}^{N} \frac{a_n}{2}(\phi_{i+n} + \phi_{i-n}) \qquad (28)$$

Equation (28) is based on templates proposed in Refs. 31 and 17 and can yield $2N$th-order formulas on a $2N+1$ point stencil. Taylor- and Fourier-series analyses are employed to derive the $N+1$ coefficients $a_0, a_1, \ldots, a_N$ in terms of α_f (see Ref. 29). Then, Eq. (28) may be written as

$$\alpha_f \hat{\phi}_{i-1} + \hat{\phi}_i + \alpha_f \hat{\phi}_{i+1} = f_{2N}(\alpha_f, \phi_{i-N}, \ldots, \phi_{i+N}) \qquad (29)$$

and α_f is the only free parameter, $-0.5 < \alpha_f \leq 0.5$, with higher values corresponding to a more dissipative filter. Computations on a range of two- and three-dimensional problems suggest that, on meshes of reasonable quality, a value $0.3 \leq \alpha_f < 0.5$ is appropriate. Only in cases where the mesh is of extremely poor quality, if it contains metric discontinuities, for example, a lower value of $\alpha_f \sim 0.1$ is required. At near boundary points, where Eq. (28) is not applicable, the approach of Ref. 10 is adopted, in which the order of accuracy is reduced on approaching the boundary. An alternative approach utilizing high-order one-sided methods may be found in Ref. 19. For multidimensional problems, the filter is applied sequentially in each of the three directions.

The physical boundary conditions are applied after each update of the interior solution vector. These include Dirichlet (no-slip) and Neumann (e.g., $\partial p/\partial n = 0$, extrapolation and symmetry) conditions and, because they are problem dependent, they are discussed in the context of each problem examined in Sec. IV. For initial conditions, uniform flow is assumed and the $\boldsymbol{B}$ field is chosen to satisfy $\nabla \cdot \boldsymbol{B} = 0$. To ensure that this condition is enforced at all times, solutions are marched in time-accurate fashion. This is accomplished with the classical fourth-order four-stage Runge–Kutta method implemented in the low-storage form of Ref. 32.

IV. Validation Cases

Several problems are now simulated to highlight the properties of the higher-order algorithm with particular focus on the new phenomena introduced due to the conducting nature of the fluid. Both steady and unsteady situations are considered. Because the primary purpose is validation, these problems are either amenable to analytic solution or have been examined extensively in the literature with other methods. For this reason, the focus here is necessarily on at most two-dimensional cases with constant conductivity. Note that the method and code based thereon is not restricted in this manner: Ref. 33 examines fully three-dimensional variable conductivity flows with the same method. Unless otherwise mentioned, all computations employ a 10th-order filter with $\alpha_f = 0.49$.

A. Alfvén Wave Propagation

The first problem simulated consists of the field perturbation caused by a transverse disturbance to an imposed magnetic field. It is well known (see, for example, Ref. 6) that magnetic field lines act as though they were under tension and, thus, support wave motion, Alfvén waves, which persist even in incompressible conducting fluids. A perfect medium is assumed, that is, the molecular viscosity is zero and the electrical conductivity is infinite (Fig. 1). The coordinate reference frame is assumed to be aligned such that x components of the magnetic and velocity fields are

$$B_x = \text{const}, \qquad u = 0 \qquad (30)$$

where it is reiterated that all quantities are nondimensional. Under these conditions, it is straightforward to show that the solution to the governing equations is $B_z\sqrt{(R_b/\mu_m\rho)}(x,t) = -w(x,t) = f(x - c_A t)$, where c_A is the wave velocity, $c_A = B_x/\sqrt{(R_b\mu_m\rho)}$ and only the rightward propagating wave is considered. The domain extends $-7.5 < x < 7.5$ and periodic end conditions are assumed in each of the three directions. The mesh consists of $51 \times 7 \times 7$ points. (Because the code is three-dimensional, a few points are required in the third direction even for nominally two-dimensional cases). The Mach number is set to the low value of 0.01 to simulate effectively incompressible flow. Numerical experiments indicate that a Δt value of 0.005 is sufficient to yield time-step-size independent results. The value of static pressure p is adjusted to maintain the constancy of $P = p + R_b(\boldsymbol{B}^2/2\mu_m)$. In all cases, R_b, μ_m, and ρ are set to unity. The nondimensional wave speed is then B_x. The disturbance is specified in terms of the B_z and w form at $t = 0$. It is assumed that a current exists to satisfy the induction equation $\nabla \times \boldsymbol{B}/\mu_m = Re_\sigma \boldsymbol{j}$. (Note that $\boldsymbol{j}$ is normalized by $\sigma_{\text{ref}} U_{\text{ref}} B_{\text{ref}}$.)

Two different traveling wave forms are considered for these simulations. The first consists of a Gaussian function $B_z\sqrt{(R_b/\mu_m\rho)}(x,0) = e^{-x^2}$. Results with three different schemes, E2, C4, and C6 are shown in Fig. 2 at time $T = 15$, that is, when the waveform has traveled once around the mesh. It is evident that the two compact schemes are far superior to the explicit scheme, which develops a tail due to the much higher dispersion error. Note that the transverse disturbances are not small, and they do not need to be because no linearization of the governing equations is necessary for this essentially incompressible simulation.

The second disturbance considered has a soliton waveform encountered frequently in plasmadynamics, $B_z\sqrt{(R_b/\mu_m\rho)}(x,0) = 3c\,\text{sech}^2[(c/2)^{1/2}x]$. The value of B_x and c_A are fixed at 2 to provide a wave moving at a phase velocity twice that of the earlier case. Δt is set to 0.001 to assure time-step-size independent results. The results with E4, C4, and C6 are shown in Fig. 3 at time $T = 7.5$. Although

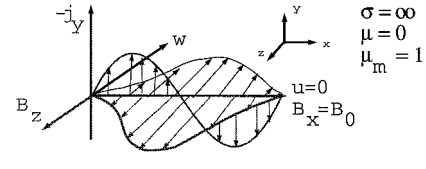

Fig. 1 Schematic of Alfvén wave propagation problem.

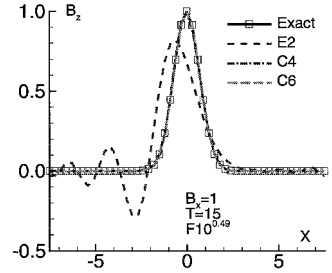

Fig. 2 Propagation of Gaussian disturbance as an Alfvén wave; $B_x = 1$.

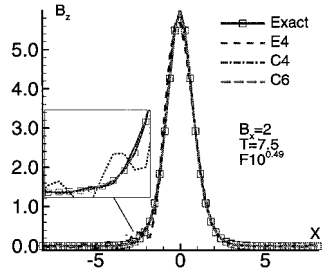

Fig. 3 Propagation of soliton waveform as an Alfvén wave; $B_x = 2$.

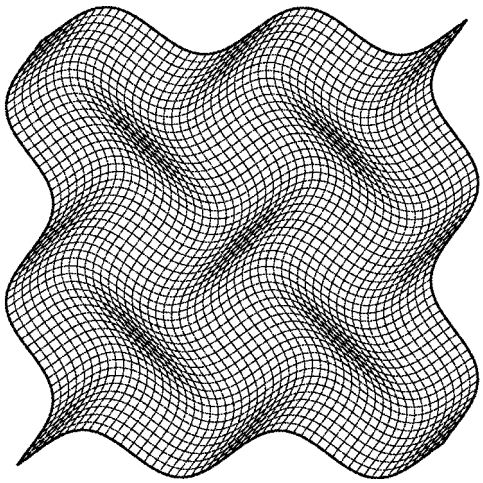

a) Wavy mesh

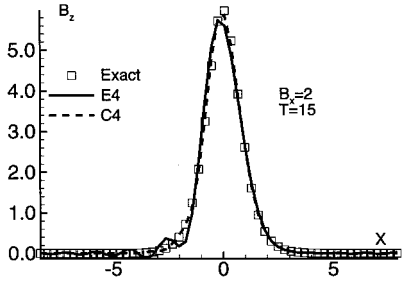

b) B_z

Fig. 4 Propagation of soliton waveform as an Alfvén wave on curvilinear mesh.

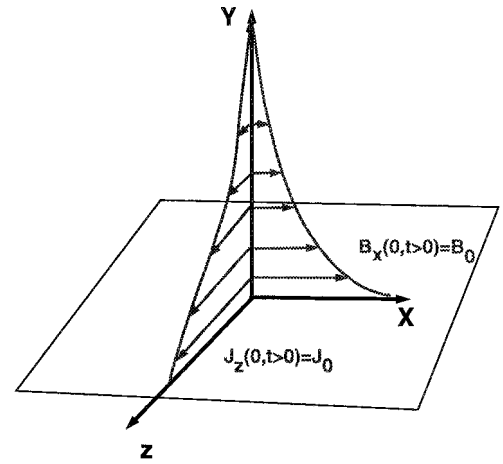

a) Schematic

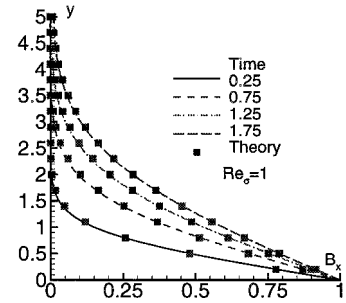

b) Diffusion at several time instants

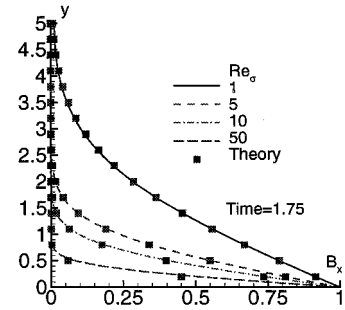

c) Effect of magnetic Reynolds number

Fig. 5 Magnetic equivalent of Rayleigh problem.

the E4 scheme is more accurate than the E2 scheme, close scrutiny reveals the anticipated dispersive (lag) error. The two compact difference based methods C4 and C6, however, are in close agreement with theory both for $\boldsymbol{B}_z$ propagation and w-velocity generation (not shown).

The performance of the algorithm on a highly curvilinear mesh is examined next by considering the wavy mesh[10,19] shown in Fig. 4a. Lines on a $51 \times 51 \times 7$ uniform mesh are distorted by the application of sinusoidal disturbances to yield a highly skewed and stretched grid. The soliton waveform is retained with $B_x = 2$. The value of B_z is plotted at $T = 7.5$ along the coordinate line corresponding to $\boldsymbol{j} = JL/2$ in Fig. 4b for E4 and C4, respectively. The C4 scheme retains its superiority and shows relatively little degradation. The E4 scheme, however, exhibits significantly more pronounced undulations. The values of $\nabla \cdot \boldsymbol{B}$ lie in machine zero range. Although this is essentially a one-dimensional problem in that no quantity varies in its own direction, the issue is nontrivial because nonnegligible values of $\nabla \cdot \boldsymbol{B}$ may arise due to the metric terms incorporated into the strong conservation form. An extensive discussion of the use of compact difference and higher-order finite difference schemes on curvilinear meshes may be found in Refs. 11 and 19.

B. Magnetic Field Diffusion

The diffusion of a magnetic field is now considered to validate the nonideal components of the code and algorithm for finitely conducting media. The problem, summarized in Fig. 5a, is chosen because of its similarity to the Rayleigh problem in fluid dynamics where an infinite surface adjoining a viscous fluid is suddenly imparted a step velocity in its own plane. For the magnetic equivalent, a current is suddenly imposed on the plane boundary of a semi-infinite region of conductivity σ. At $t = 0$, a sheet current $j_z(0, t > 0) = j_0$ flows on the surface. Outside the conductor, this current induces a uniform magnetic field $B_x(0, t > 0) = B_0$ parallel to the surface. The frame of reference is chosen such that the conductor is stationary, and, initially, there is no field inside the conductor. Thus, longitudinal waves are not supported, and the solution to the problem requires only the specification of $B_x(y, t)$. The boundary conditions on the surface are enforced by specifying the no-slip condition together with the specified value of B_x with $B_y = B_z = 0$. The outer boundary is placed far away, and a zero gradient condition is specified there. The discretization employs 100 points in $0 < y < 10$. Again, seven points each are employed in the directions of no variation, x and y, respectively, and Δt is fixed at a low value (0.001) to assure time-step-size independent results.

Figure 5b plots the B_x field at several time instants for $Re_\sigma = 1$. The square symbols mark theoretical values obtained by solving the governing equations under the aforementioned boundary conditions. Note that, for clarity, in Fig. 5 and subsequent figures, theoretical values are plotted only at a subset of the grid points in the solution. The solution procedure is similar to that for the fluid dynamic Rayleigh problem. Introducing a similarity parameter

$y/2\sqrt{(t/Re_\sigma)}$, the solution for $B_0 = 1$ is obtained in terms of the complimentary error function

$$B_x = 1 - \frac{2}{\pi}\int_0^{\frac{y}{2\sqrt{t/Re_\sigma}}} e^{-\xi^2}\,\mathrm{d}\xi \tag{31}$$

Despite the action at a distance nature of electromagnetic forces, the magnetic field diffuses into the conductor at a finite rate in perfect analogy to the effect of plate motion in the fluid dynamic case. As noted in Ref. 6, this is the effect of countercurrents induced in the conductor as a consequence of Lenz's law. To highlight this phenomenon, Fig. 5c shows the diffusion of the field into the conductor at a fixed time $t = 1.75$ for various magnetic Reynolds numbers. Again, the computations are indistinguishable from the theoretical result. At higher magnetic Reynolds numbers (higher conductivity), the induced currents are larger and shield the interior regions to a greater extent. In the limit of perfect conductivity, this trend confirms the expectation that the external excitation is completely shielded from the interior.

C. Alfvén Waves with Ohmic Damping

The next case considers the propagation of transverse Alfvén waves in a medium of finite conductivity (see, for example, Ref. 6). In this case, the medium is disturbed by the application of a sinusoidally oscillating current j_y (Fig. 6a). The coordinate frame is again chosen to fix $u = 0$ and $B_x = 1$. The transverse disturbance then travels along the x direction, ultimately decaying due to damping associated with the finite conductivity of the medium.

The problem has an analytical solution of the form $B_z = Ae^{i(\omega t + kx)}$ and $w = Ce^{i(\omega t + kx)}$, where ω, the frequency, and A, the amplitude, are known (imposed) and $i = \sqrt{-1}$. C and k are determined by inserting this assumed solution into the governing equations after setting the molecular viscosity μ to zero. The expressions for k and C for the domain $x > 0$ are given in Ref. 6. At $x = 0$, the effect of the imposed current is enforced when the values of B_z and w are set to match the real components of the preceding solutions, while the gradients of all other quantities are set to zero. The right boundary is situated at $x = 20$, where all field values are extrapolated with a simple second-order formula. At the end of each iteration, the static pressure is adjusted to satisfy the constraint $P = p + (R_b/2\mu_m)\boldsymbol{B}\cdot\boldsymbol{B} =$ const to track the irrotational component of the Maxwell stress at each point.

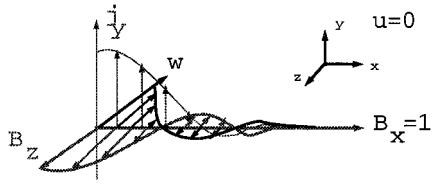

a) Schematic

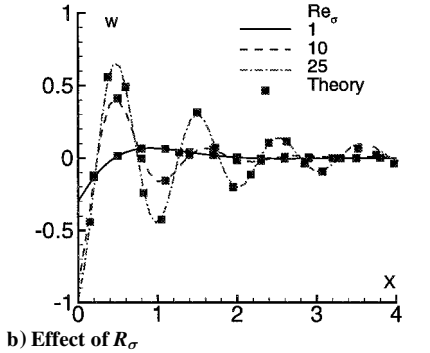

b) Effect of R_σ

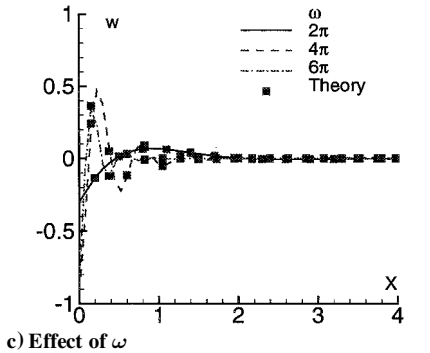

c) Effect of ω

Fig. 6 Alfvén waves with ohmic damping.

The accuracy of the scheme in reproducing the basic phenomena of interest is depicted in Figs. 6b and 6c, which show the effect of magnetic Reynolds number and frequency of excitation ω on the transverse w velocity at time $t = 4$ on a $100 \times 7 \times 7$ mesh. The parameter of relevance in such problems is $\rho\omega/\sigma B_x^2$, which is inversely proportional to the Lundquist number. Because the Alfvén speed is normalized to unity, the leading edge of the disturbance is at $x = 4$ at this instant. As the conductivity is increased (higher R_σ), the waves penetrate deeper into the medium before being damped out. The numerical simulation retains the plane, transverse nature of the phenomenon. This is manifested by the absence of any induced velocity in the x or y direction (not shown). At the lowest value of R_σ, the disturbance decays nearly monotonically. The computations recover the similarity between conductivity for magnetic terms and the reciprocal of molecular viscosity for viscous stresses. In the limit of perfect conductivity, the asymptote of the undamped Alfvén wave is recovered. The impact of increasing the frequency of excitation ω is exhibited in Fig. 6c. At higher frequencies, the signal decays relatively rapidly because fluid inertia inhibits reaction to the rapid oscillations. In contrast, at very low frequencies, the Lundquist number is large. In this case, waves are only weakly damped and propagate many wavelengths into the medium before decaying.

This example demonstrates the ability of the method to reproduce that Maxwell's stresses can generate vorticity ($\partial w/\partial x \neq 0$), as well as to convect vorticity in a direction parallel to a component of the magnetic field. The importance of this aspect of MGD interaction is reflected in the potential implication on the dynamics and control of turbulence, in which vorticity plays a crucial role.

D. Magnetic Shock Tube

The shock-tube problem is chosen as a representative example of a compressible flow. The initial condition consists of two states separated by a diaphragm as illustrated in Fig. 7. The parameters are taken from the work of Brio and Wu[7]. The method described in Sec. III, if employed without modification, requires a second-order filter for stability, resulting in a highly diffusive scheme. To capture shocks more accurately, the following simple algorithm is introduced to lower the filter order of accuracy to two only locally near shocks, while retaining the higher-order baseline filter everywhere. The difference scheme is not modified. For the present purpose, it is sufficient to introduce an on–off shock detection switch at each point (i, χ_i,) whose value is one if a shock exists and zero otherwise. To obtain χ_i, a sharp variation detection formula is adapted from the work of Harten[34] and Yee[35]:

$$\hat{\chi}_i = \begin{cases} 1 & \text{if } \left|\dfrac{|\Delta_{i+1}\Phi| - |\Delta_i\Phi|}{|\Delta_{i+1}\Phi| + |\Delta_i\Phi| + \delta}\right| > \epsilon \\ 0 & \text{otherwise} \end{cases}$$

$$\chi_i = \max(\hat{\chi}_{i-1}, \hat{\chi}_i, \hat{\chi}_{i+1}) \tag{32}$$

where $\Delta_i = \Phi_i - \Phi_{i-1}$. Several possibilities exist to define Φ in terms of the primitive variables: For simplicity, the results described here employ $\Phi = u$, ϵ is fixed at 0.2, and δ is a small number to prevent division by zero in regions of no variation ($\delta = 1 \times 10^{-10}$).

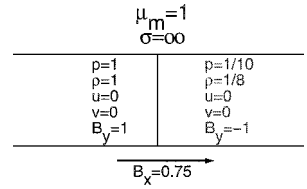

Fig. 7 Schematic of shock-tube configuration.

Then χ_i is employed to reduce locally the filter order of accuracy to two by replacing the filter formula, Eq. (29), by

$$\alpha_f\hat{\phi}_{i-1} + \hat{\phi}_i + \alpha_f\hat{\phi}_{i+1} = \chi_i f_2(\alpha_f, \phi_{i-1}, \phi_i, \phi_{i+1}) + (1-\chi_i) f_{2N}(\alpha_f, \phi_{i-N}, \ldots, \phi_{i+N}) \quad (33)$$

where f_2 and f_{2N} are the right-hand sides of Eq. (28) for the second and baseline higher-order filter, respectively.

The computed profiles for ρ, p, u, v, and B_y, utilizing the C4 scheme together with the eighth-order accurate ($\alpha_f = 0.3$) baseline filter, are shown in Fig. 8. The mesh and time-step size are the same as those employed by Brio and Wu[7]: 800 points are considered spaced $\Delta x = 1$ apart and the time-step size is fixed at $\Delta t = 0.2$. Each of the five features noted in Ref. 7 are marked in the density plot: Features propagating to the left include the fast rarefaction and the slow compound wave, whereas those propagating to the right include the contact discontinuity, the slow shock, and the fast rarefaction. The jumps in various quantities also compare favorably with results published in the literature. The discontinuous features are only slightly more smeared than when upwind methods are used. In this case, the moving shock has about four points inside it: this is only one point more than observed in the results of Ref. 7. No overshoots are evident in the pressure, density, or B_y fields, although a modest oscillation is evident near the slow shock in the u and v fields. These can be eliminated by a more conservative (lower) choice of ϵ in the preceding shock-capturing formulation (not shown). One interesting aspect that emerges from the solution is the presence of a v velocity and a vorticity component associated with its x variation caused by the waves noted earlier. A discussion of the stability of the component structures in the presence of multidimensional disturbances may be found in Ref. 23.

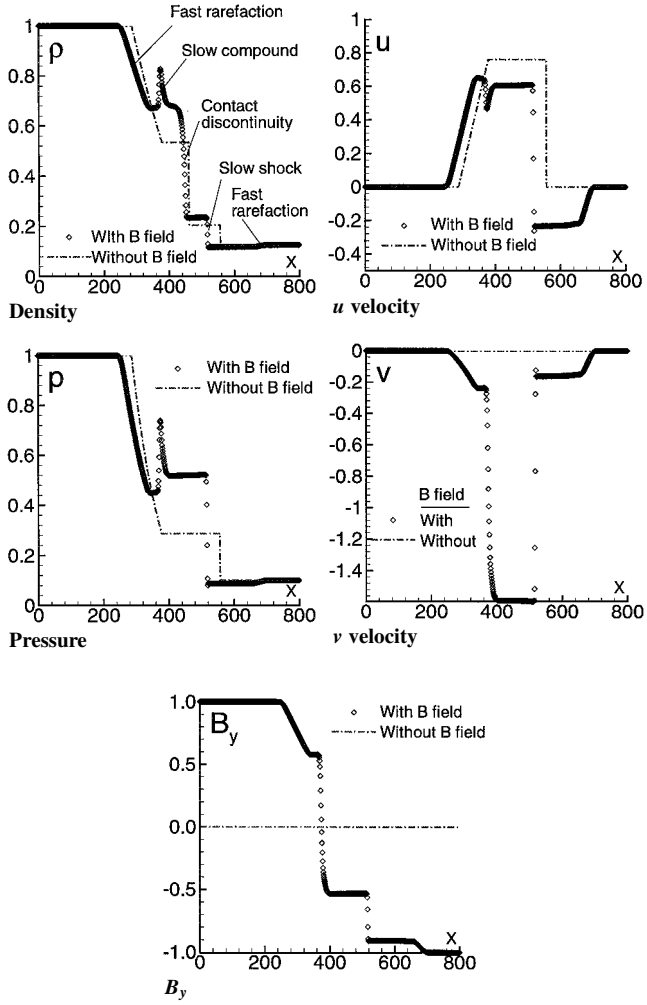

Fig. 8 MGD shock-tube simulation.

E. Hartmann Flows

As noted in the Introduction, electromagnetic devices, such as generators and accelerators, offer many potential possibilities in improving the efficiency of propulsion in hypersonic flight. In generators, energy is extracted from a moving conducting flow, whereas in pumps, fluid momentum is enhanced by energy transfer to it. From a numerical standpoint, the problem requires careful simulation of the interaction between electromagnetic, pressure, and viscous forces. The pertinent parameter in such flows is the Hartmann number, $Ha = \sqrt{(Re Re_\sigma R_b)} = B_{\text{ref}} L \sqrt{(\sigma_{\text{ref}}/\mu_{\text{ref}})}$, which is a measure of the ratio of magnetic to viscous forces. The configuration is depicted in Fig. 9a together with a simplified representation of the circuit completing the current path. The dimensions of the channel transverse to the flow are assumed to have a high aspect ratio, that is, $W/(2H) \gg 1$, so that end effects can be ignored in the study of the flow in the vicinity of the center of the channel. A uniform magnetic field is imposed in the y direction ($B_y = 1$), and an electric field, measured by the nondimensional parameter $K = -E_z/(U_{\text{ref}} B_{\text{ref}})$, is imposed across the channel. Of the several simulated devices possible with this setup, we consider the pump and the generator at a Hartmann number of 100. For generators, $0 < K < 1$: The value chosen for this study is $K = 0.5$, the so-called impedence match case, in which the external load and fluid electrical resistance are equal and maximum power is extracted. The fluid experiences a favorable pressure gradient and current flows in the $+z$ direction (Fig. 9b). Values of K for pumps exceed one: In this work a representative value of two is chosen. In this case, fluid is pumped against an adverse pressure gradient and current flows in the $-z$ direction.

To facilitate comparison with theory, the system is assumed to be compensated that is, the constant y component of the magnetic field is unperturbed. This is achieved by assuring that B_x is the only induced field and requires that current return paths be provided alongside the channel walls[6] as depicted schematically in Fig. 9b.

The problem is modeled by considering a finite streamwise length of the channel. The boundary conditions are now described in detail

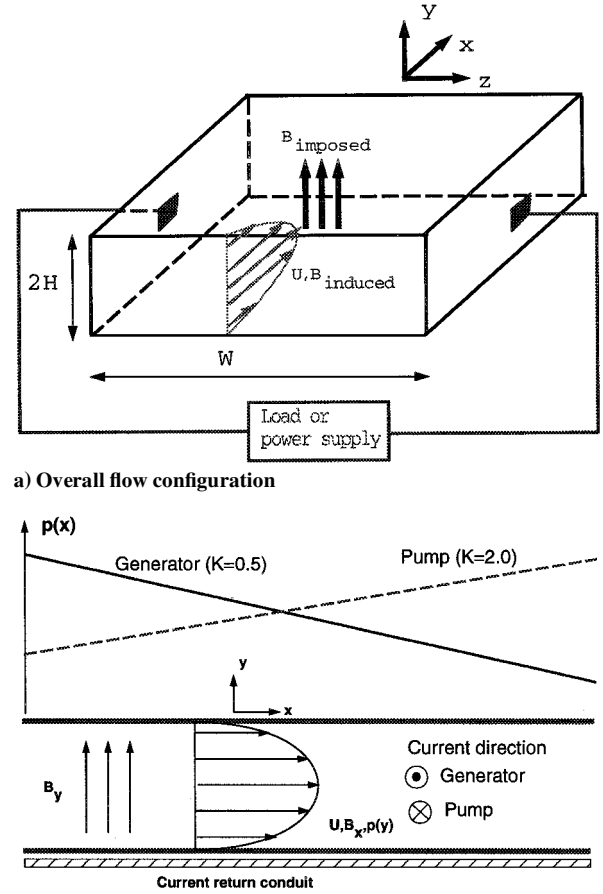

Fig. 9 Hartmann flow.

because some aspects are common to many problems of interest where an internal or external boundary layer interacts with a magnetic field. The no-slip condition dictates zero velocity components on the channel walls. The effect of the external load is imposed through the value of the induced B_x field at the channel walls in the following manner. From Ohm's law, the total current across the channel is

$$J_{\text{cur}} = \int_{-1}^{1} j\,\mathrm{d}y = \int_{-1}^{1} Re_\sigma \sigma(-K + U \times \boldsymbol{B})\,\mathrm{d}y$$
$$= Re_\sigma(-2K + Q_f B_y) \tag{34}$$

where Q_f is the nondimensional flow rate, which is chosen to be two, that is, the mean velocity is unity. In the preceding equation, σ has been assumed to be constant. Variable conductivity is easy to incorporate in this development as shown in Ref. 33. From Ampere's law,

$$J_{\text{cur}} = \int_{-1}^{1} \nabla \times \boldsymbol{B}\,\mathrm{d}y = \int_{-1}^{1} \frac{\partial B_x}{\partial y}\,\mathrm{d}y = 2B_{x,\text{wall}} \tag{35}$$

where the fact that the induced field is symmetric about the centerline has been used. Equations (34) and (35) yield the required value of $B_{x,\text{wall}}$ because K, Q_f, and B_y are known (chosen). To obtain pressure at the walls, the balance of forces normal to the wall is considered, that is,

$$\frac{\partial}{\partial n}\left[\bar{\tau}_n - \left(B_n - \frac{\boldsymbol{B}\cdot\boldsymbol{B}}{2\mu_m}\right)\right] = 0 \tag{36}$$

where $\bar{\tau}_n$ is the normal component of the stress tensor including static pressure, and n denotes the direction normal to the wall. The condition $\nabla \cdot \boldsymbol{B} = 0$ yields $\partial B_n/\partial n = 0$, which follows in a straightforward fashion by application of Gauss's divergence law to a volume straddling the wall. If $\bar{\tau}_n$ is assumed to be the static pressure p, an assumption that is valid for inviscid flows and to a large extent for boundary-layer flows, then the wall pressure p_w may be obtained from

$$\frac{\partial[p_w + (\boldsymbol{B}\cdot\boldsymbol{B}/2\mu_m)]}{\partial n} = 0 \tag{37}$$

because all components of $\boldsymbol{B}$ have already been determined. The density can then be obtained for isothermal or adiabatic walls from

$$\rho_w = \gamma M^2 (p_w/T_w) \tag{38}$$

or

$$\frac{\partial \rho_w}{\partial n} = 0 \tag{39}$$

respectively. In the streamwise direction, periodic conditions are employed for all quantities except static pressure, whose gradient is specified at each boundary to match the chosen Reynolds number, as well as K and Ha:

$$\frac{\partial p}{\partial x} = \left[K - \left(\frac{Ha}{Ha - \tanh[Ha]}\right)\right]\frac{Ha^2}{Re} \tag{40}$$

Periodicity is enforced on all quantities in the spanwise direction.

Figure 10 exhibits the velocity profile obtained with the compact fourth-order scheme together with the eighth-order filter for $K = 2$ (pump) and $Ha = 100$ ($Re = 100$, $R_b = 10$, and $Re_\sigma = 10$). The velocity profile without the $\boldsymbol{B}$ field is also shown together with the theoretical result, the equation for which may be found in Ref. 24. Three different meshes are considered consisting of $30 \times 50 \times 5$, $50 \times 80 \times 5$, and $50 \times 110 \times 5$ points. Each mesh is stretched in the vertical direction: The finest mesh has a minimum spacing of $\Delta y = 0.00005$ and contains about 35 points in each Hartmann layer. It is evident that the two coarser meshes exhibit error near the edge of the Hartmann layer (see insert of Fig. 10). These mesh resolution requirements are substantially more stringent than in the more benign case examined in Ref. 36, where the Hartmann number was fixed at 10 and a uniform mesh was found to be sufficient. In comparison with the case where no $\boldsymbol{B}$ field is applied, the effect of the magnetic field is to flatten the velocity as expected because $\boldsymbol{j} \times \boldsymbol{B}$ forces diminish shear. Only near the channel walls, where velocity gradients are high, are viscous stresses of the same order as the Maxwell stresses.

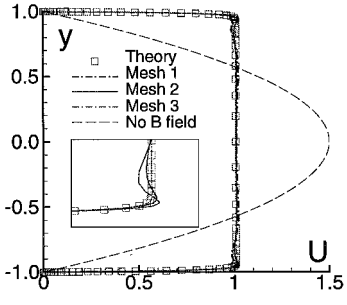

Fig. 10 Velocity profiles in Hartmann flow simulation at $Ha = 100$ and $K = 2$.

The velocity profile shown in Fig. 10 is a function only of the Hartmann number when the flow rate is fixed because there is then a direct relationship between K, $\partial p/\partial x$, and the Reynolds number. The induced magnetic field, however, depends on both K and the Reynolds number Re_σ. This dependence is illustrated in Figs. 11a and 11b, respectively. In the first, the variation of B_x on the finest mesh is plotted vs y for the pump and generator. The induced magnetic field varies almost linearly across the channel and is symmetric about the centerline. The computations reproduce theory quite accurately. Discrepancies are modest and are observed principally in the vicinity of the centerline of the channel, where the stretched mesh is relatively coarse; the spacing may be discerned from the marker locations for the theoretical result. The slopes of the curves are proportional to the current and are of different signs for the two cases. This reflects that in the pump, the current is opposed to the $U \times \boldsymbol{B}$ component in Ohm's law due to the large negative value of E_z because $K = -E_z/U_{\text{ref}}\,B_{\text{ref}}$. In contrast, the current in the generator is parallel to $U \times \boldsymbol{B}$ but is smaller than in the short-circuit ($K = 0$) case (not simulated), and work is done by the fluid against the electrical load. The effect of the Reynolds number Re_σ on the induced field is depicted for the case of the pump in Fig. 11b, where the values of the Reynolds number Re_b and Re_σ are varied in a manner that maintains the value of the Hartmann number at 100. Although the velocity profile is unchanged from that plotted in Fig. 10 (not shown), the magnitude of the induced field is directly dependent on the Reynolds number Re_σ, as is the current that is proportional to $\partial B_x/\partial y$.

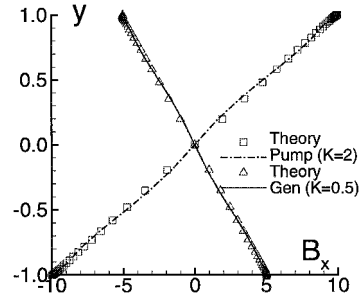

a) Variation with K

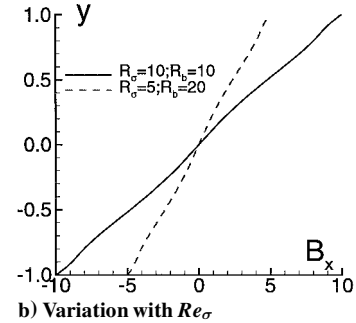

b) Variation with Re_σ

Fig. 11 Induced magnetic field at $Ha = 100$.

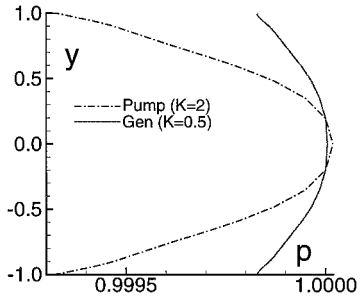

Fig. 12 Pressure variation across channel for *Ha* =100.

The final aspect examined is that related to the boundary condition at the channel walls. Figure 12 exhibits the variation of pressure across the channel. It is evident that the normal gradient of pressure near the wall is not zero as in the non-MGD case, but is rather related to the variation of current as determined by Eq. (37). Numerical experiments suggest that inaccurate implementation of this boundary condition can affect the assumption of compensation and introduce spurious perturbations in the imposed B_y component of the magnetic field.

V. Conclusions

A higher-order compact difference based method has been adapted to solve the governing equations of nonideal MGD. The components of the scheme include 4th- and 6th-order derivative formulas together with up to 10th-order filters, which are required to maintain stability in the presence of mesh stretching, discretely applied boundary conditions, and nonlinearities. For shock waves, a simple extension based on a switching mechanism is developed to capture moving shocks with a lower-order filter, while retaining the high accuracy of the baseline scheme in smooth regions. Each of the components of the scheme is versatile in that it is easily applied to more complicated governing equations with minimal effort. The method is validated for MGD by solving a wide range of problems for which either analytic results are available or that have been simulated with other methods. These cases distill the various phenomena of interest in the simulation of finitely conducting flow in the presence of magnetic fields and include wave propagation as well as steady-state situations. The results demonstrate that the scheme exhibits an excellent blend of properties and is superior to lower-order variants.

Acknowledgments

The author is grateful for Air Force Office of Scientific Research sponsorship under tasks monitored by W. Hilbun and S. Walker. This work was also supported in part by a Grant of High Performance Computing (HPC) time from the U.S. Department of Defense HPC Shared Resource Centers at the Corps of Engineers, Waterways Engineering Station, and the Naval Oceanographic Office. The author acknowledges several useful conversations with M. Aftosmis, D. Gottlieb, J. Poggie, R. MacCormack, J. Shang, C.-W. Shu, M. Visbal, H. Yee, and J. Young.

References

[1]Ziemer, R. W., and Bush, W. B., "Magnetic Field Effects on Bow Shock Stand-Off Distance," *Physical Review Letters*, Vol. 1, No. 2, 1958, pp. 58, 59.

[2]Meyer, R. X., "Magnetohydrodynamics and Aerodynamic Heating," *ARS Journal*, Vol. 29, No. 3, 1959, pp. 187–192.

[3]Gurijanov, E. P., and Harsha, P. T., "AJAX: New Directions in Hypersonic Technology," AIAA Paper 96-4609, Nov. 1996.

[4]Brichkin, D. I., Kuranov, A. L., and Sheikin, E. G., "MHD-Technology for Scramjet Control," AIAA Paper 98-1642, April 1998.

[5]Ganiev, Y. C., Gordeev, V. P., Krasilnikov, A. V., Lagutin, V. I., Otmennikov, V. N., and Panasenko, A. V., "Theoretical and Experimental Study of the Possibility of Reducing Aerodynamic Drag by Employing Plasma Injection," AIAA Paper 99-0603, Jan. 1999.

[6]Shercliff, J. A., *A Textbook of Magnetohydrodynamics*, Pergamon, Oxford, 1965.

[7]Brio, M., and Wu, C. C., "An Upwind Differencing Scheme for the Equations of Ideal Magnetohydrodynamics," *Journal of Computational Physics*, Vol. 75, No. 2, 1988, pp. 400–422.

[8]Powell, K. G., Roe, P. L., Myong, R. S., Gombosi, T., and Zeeuw, D. D., "Upwind Scheme for Magnetohydrodynamics," AIAA Paper 95-1704, June 1995.

[9]Myong, R. S., and Roe, P. L., "On Godunov-Type Schemes for Magnetohydrodynamics," *Journal of Computational Physics*, Vol. 147, No. 2, 1998, pp. 545–567.

[10]Visbal, M. R., and Gaitonde, D. V., "High-Order Accurate Methods for Complex Unsteady Subsonic Flows," *AIAA Journal*, Vol. 37, No. 10, 1999, pp. 1231–1239.

[11]Visbal, M. R., and Gaitonde, D. V., "Computation of Aeroacoustic Fields on General Geometries Using Compact-Differencing and Filtering Schemes," AIAA Paper 99-3706, June 1999.

[12]Augustinus, J., Hoffmann, K. A., and Harada, S., "Numerical Solutions of Ideal MHD Equations for a Symmetric Blunt Body at Hypersonic Speeds," AIAA Paper 98-0850, Jan. 1998.

[13]MacCormack, R. W., "Upwind Conservation Form Method for the Ideal Magnetohydrodynamics Equations," AIAA Paper 99-3609, June 1999.

[14]Jones, O. S., Shumlak, U., and Eberhardt, D. S., "An Implicit Scheme for Nonideal Magnetohydrodynamics," *Journal of Computational Physics*, Vol. 130, No. 1, 1997, pp. 231–242.

[15]MacCormack, R. W., "Numerical Computation in Magnetofluid Dynamics," *CFD for the 21st Century*, Japan Society for Aeronautical and Space Sciences, Tokyo, 2000.

[16]Hirsh, R. S., "Higher Order Accurate Difference Solutions of Fluid Mechanics Problems by a Compact Differencing Technique," *Journal of Computational Physics*, Vol. 19, No. 1, 1975, pp. 90–109.

[17]Lele, S. K., "Compact Finite Difference Schemes with Spectral-Like Resolution," *Journal of Computational Physics*, Vol. 103, 1992, pp. 16–42.

[18]Gaitonde, D. V., Shang, J. S., and Young, J. L., "Practical Aspects of High-Order Accurate Finite Volume Schemes for Electromagnetics," AIAA Paper 97-0363, Jan. 1997.

[19]Gaitonde, D. V., and Visbal, M. R., "Further Development of a Navier–Stokes Solution Procedure Based on Higher-Order Formulas," AIAA Paper 99-0557, Jan. 1999.

[20]Rizzetta, D. P., Visbal, M. R., and Blaisdell, G. A., "Application of a High-Order Compact Difference Scheme to Large-Eddy and Direct Numerical Simulation," AIAA Paper 99-3714, June 1999.

[21]Rizzetta, D. P., Visbal, M. R., and Gaitonde, D. V., "Direct Numerical and Large-Eddy Simulation of Supersonic Flows by a High-Order Method," AIAA Paper 2000-2408, 2000.

[22]Rankin, R. R., Self, S. A., and Eustis, R. H., "Study of the Insulating Wall Boundary Layer in a Faraday MHD Generator," *AIAA Journal*, Vol. 18, No. 9, 1980, pp. 1094–1100.

[23]Barmin, A. A., Kulikovskiy, A. G., and Pogorelov, N. V., "Shock-Capturing Approach and Nonevolutionary Solutions in Magnetohydrodynamics," *Journal of Computational Physics*, Vol. 126, No. 1, 1996, pp. 77–90.

[24]Jeffrey, A., *Magnetohydrodynamics*, Oliver and Boyd, Edinburgh, 1966.

[25]Anderson, D. A., Tannehill, J. C., and Pletcher, R. H., *Computational Fluid Mechanics and Heat Transfer*, McGraw–Hill, New York, 1984.

[26]Gaitonde, D. V., and Shang, J. S., "Optimized Compact-Difference-Based Finite-Volume Schemes for Linear Wave Phenomena," *Journal of Computational Physics*, Vol. 138, No. 2, 1997, pp. 617–643.

[27]Collatz, L., *Numerical Treatment of Differential Equations*, 3rd ed., Springer-Verlag, Berlin, 1966.

[28]Carpenter, M. H., Gottlieb, D., and Abarbanel, S., "The Stability of Numerical Boundary Treatments for Compact High-Order Finite-Difference Schemes," NASA CR 187628 Sept. 1991; also Inst. for Computer Applications in Science and Engineering, Rept. 91-71, Hampton, VA, Sept. 1991.

[29]Gaitonde, D. V., and Visbal, M. R., "High-Order Schemes for Navier–Stokes Equations: Algorithm and Implementation into FDL3DI," U.S. Air Force Research Lab, TR AFRL-VA-WP-TR-1998-3060, Wright–Patterson AFB, OH, 1998.

[30]Thompson, J. F., Warsi, Z. U. A., and Mastin, C. W., *Numerical Grid Generation*, North-Holland, New York, 1985.

[31]Alpert, P., "Implicit Filtering in Conjunction with Explicit Filtering," *Journal of Computational Physics*, Vol. 44, No. 1, 1981, pp. 212–219.

[32]Fyfe, D. J., "Economical Evaluation of Runge–Kutta Formulae," *Mathematics of Computation*, Vol. 20, No. 95, 1966, pp. 392–398.

[33]Gaitonde, D. V., and Poggie, J., "Simulation of Magnetogasdynamic Flow Control Techniques," AIAA Paper 2000-2326, 2000.

[34]Harten, A., "The Artificial Compression Method for Computation of Shocks and Contact Discontinuities: III. Self-Adjusting Hybrid Schemes," *Mathematics of Computation*, Vol. 32, No. 142, 1978, pp. 363–389.

[35]Yee, H. C., "Low-Dissipative High-Order Shock-Capturing Methods Using Characteristic-Based Filters," *Journal of Computational Physics*, Vol. 150, No. 1, 1999, pp. 199–210.

[36]Gaitonde, D. V., "Development of a Solver for Three-Dimensional Nonideal Magnetogasdynamics," AIAA Paper 99-3610, June 1999.

P. Givi
Associate Editor